THE COMPLETE ANALYSIS OF A 91.33 TO 274 GHz SCHOTTKY BARRIER VARACTOR FREQUENCY TRIPLER

R. E. Lipsey, C. Mann[1], S. H. Jones, and J. Thornton[1]

Department of Electrical Engineering, University of Virginia, Charlottesville, VA 22903
[1]Millimeter Wave Technology Group, Rutherford Appleton Laboratory, Chilton, Didcot, U.K.

Abstract

A complete analysis of a SBV frequency tripler has been performed. This analysis was achieved through the development of a unique tripler block based on the mounting structure proposed by Eisenhart and Khan. Using the boundary conditions imposed by Eisenhart and Khan, an analytical model of the waveguide structure was derived and simulated. With the linear RF circuit decomposed into an analytical model, the Drift-Diffusion Harmonic-Balance numerical simulator was used to accurately model the performance of the active non-linear device in the linear embedding circuit. The results of the RF circuit simulations combined with the numerical device Harmonic-Balance simulator is then compared to experimental results and demonstrates a high degree of accuracy over a wide range of output backshort positions.

I. Introduction

In the drive to create solid-state heterodyne mixers at frequencies above 1 THz, the provision of sufficient local oscillator power becomes a critical issue [1]. Since substantial power has been reported from solid-state LO chains around 300 GHz (6-8 mW) [2 -3], a final tripler stage using a Schottky Barrier Varactor diode (SBV) with an efficiency of 6% would provide enough power to drive a single-diode harmonic mixer at frequencies near 2 THz. There are, however, significant difficulties in the design of triplers at these high frequencies. These difficulties include the design of the Schottky device, idlers and filters, as well as reliable and reproducible RF circuits to effectively couple power to and from the multiplier diode. In order to effectively couple the power into and generate power from the SBV frequency tripler, the embedding impedances of the RF circuit must be carefully designed relative to the diode. The analysis of traditional tripler waveguide structures requires the use of such programs as Hewlett Packard's High Frequency Structure Simulator (HFSS). However, simulations run for such complex structures in HFSS are extremely CPU intensive. In an attempt to create a tripler waveguide structure that lends itself to straight-forward analytical calculations for the embedding circuit impedances, a mounting waveguide based on the structure proposed by Eisenhart and Khan [4] has been developed [1], and reported here. Using the boundary conditions imposed by Eisenhart and Khan, an analytical model of the waveguide structure was derived and simulated in Mathematica. The embedding impedances presented by the linear RF circuit were calculated over a wide range of backshort positions in a matter of minutes. With the linear RF circuit decomposed into an analytical model, Computer Aided Design (CAD) techniques can be used to accurately model the performance of the active nonlinear device in the linear embedding circuit.

In this paper, we report on the use of the novel fully self-consistent physics based large signal time- and temperature-dependent Drift-Diffusion Harmonic-Balance (DDHB)

[5-6] analysis of the active device combined with the electromagnetic modeling of the waveguide based on the Eisenhart and Khan analysis. The DDHB simulator models carrier transport through the bulk region of the SBV by a set of coupled nonlinear differential equations and requires that the linear RF circuit embedding impedances be known. The combination of these tools has, for the first time, provided a means for the complete analysis of a high frequency tripler. The results of the RF circuit simulations combined with the CAD programs are compared to the experimental results for the 91.33 to 274 GHz tripler block. These results demonstrate a high degree of accuracy over a wide range of backshort positions and predict similar output powers to experimental results (i.e. 2.5 mW at 274 GHz).

II. The Tripler Waveguide Structure

The diode mount used in this work was a 230 to 290 GHz tripler based closely on the structure reported in [7]. The block employed the use of crossed LO and output waveguides, backshort and E-plane LO tuners, a backshort for output tuning, a single diode with facility for d.c. bias, and two quarter-wave transformer sections between the idler and the output waveguide. Figure 1 presents a detailed diagram of the internal configuration of the tripler waveguide structure used. The input power from the LO is coupled into the SBV via a waveguide probe, and a stripline filter on the probe prevents power at the higher harmonics from leaking back into the input waveguide. The diode is mounted in the idler waveguide approximately a quarter wavelength (at the fundamental LO frequency) from the idler to output waveguide transition in which only the fundamental LO frequency is in cut-off. The idler serves as a resonant cavity in which a standing wave in the second harmonic exists but cannot propagate into the output waveguide. The two transformers transition the idler into the output waveguide and serve to increase the circuit bandwidth. D.C. bias is provided to the device via a 140 Ω transmission line bias filter.

To create a waveguide circuit for the SBV in which the embedding impedances can be set and optimized with a high degree of confidence, the mounting structure was designed based on the waveguide proposed by Eisenhart and Khan [4] (shown in figure 2). This was accomplished by mounting the SBV to the rectangular output waveguide by connecting the waveguide wall to the diode via a thin quasi-two dimensional post. This is analogous to the rectangular waveguide structure proposed by Eisenhart and Khan and the reduced mathematical structure is shown in figure 3. By using this precise geometry, the mathematical analysis of Eisenhart and Khan can be used to accurately and quickly calculate the diode embedding impedance. Multiplier waveguide circuits have not previously been designed using a quasi-two dimensional post; hence, the method of Eisenhart and Khan could not be accurately implemented.

A very brief derivation of the embedding impedance as calculated for this structure (figure 3) using the method of [4] follows. The restrictions $w' < 0.25$ and $g' < 0.25$ on the dimensions of the waveguide structure apply. The embedding impedance is found from the combination of the impedance of the waveguide structure (the mode pair impedance), the degree of coupling between the post and the gap for a given mode pair, and the waveguide terminations with non-zero reflection.

The mode pair impedance (the series combination of the TE_{mn} and the TM_{mn} contributions) for the waveguide structure is given by

$$Z_{mn} = \frac{j\eta b}{ak} \frac{(k^2 - k_y^2)}{(2-\delta_0)(k_x^2 + k_y^2 - k^2)^{1/2}} \tag{1}$$

where

$k_x = \frac{m\pi}{a}$ $k_y = \frac{n\pi}{b}$ $k = \frac{2\pi}{\lambda}$ λ = free space wavelength

η = characteristic impeance of free space

$\delta_0 = 1$ if n = 0

$\delta_0 = 0$ if n $\neq$ 0.

The parameters *a* and *b* define the waveguide geometry. As can be seen in equation (1), Z_{mn} is only a function of *m, n*, and the waveguide geometry.

The degree of coupling between the post and the gap to a particular mode pair impedance is given by the coupling factors which are defined as

$$\text{post coupling factor} \quad k_{pm} = \sin k_x s \left(\frac{\sin\theta_m}{\theta_m} \right) \quad \text{where } \theta_m = \frac{m\pi w}{2a} \tag{2}$$

$$\text{gap coupling factor} \quad k_{gm} = \cos k_y h \left(\frac{\sin\phi_n}{\phi_n} \right) \quad \text{where } \phi_n = \frac{n\pi g}{2b} \tag{3}$$

Since the waveguide may be terminated under non-matched conditions, the following expression results for a terminated mode pair impedance $Z_{Tmn} = Z_{mn}\tau$ where

$$\tau = \frac{1 + \rho_{1mn}\exp(-2\Gamma_{mn}l_1) + \rho_{2mn}\exp(-2\Gamma_{mn}l_2) + \rho_{1mn}\rho_{2mn}\exp(-2\Gamma_{mn}(l_1 + l_2))}{1 - \rho_{1mn}\rho_{2mn}\exp(-2\Gamma_{mn}(l_1 + l_2))} \tag{4}$$

$\Gamma_{mn} = (k_x^2 + k_y^2 - k^2)^{1/2}$

ρ_{1mn} and ρ_{2mn} are the complex reflection coefficients at terminations 1 and 2

l_1 and l_2 are the distances to terminations 1 and 2 from the post (see l_1 and l_2 in figure 1(a)).

The total gap impedance, Z_{gap}, is the parallel combination of all mode pairs and is given by

$$Z_{gap} = \frac{1}{\sum_{n=0}^{N_1} \frac{1}{\sum_{m=1}^{M_1} Z_{Tmn} \left(\frac{k_{pm}}{k_{gn}}\right)^2}} \tag{5}$$

where M_1 and N_1 are the truncated limits of summation for the n and m modes, respectively. Typical values for millimeter wave devices are $M_1 = 12$ and $N_1 = 8$.

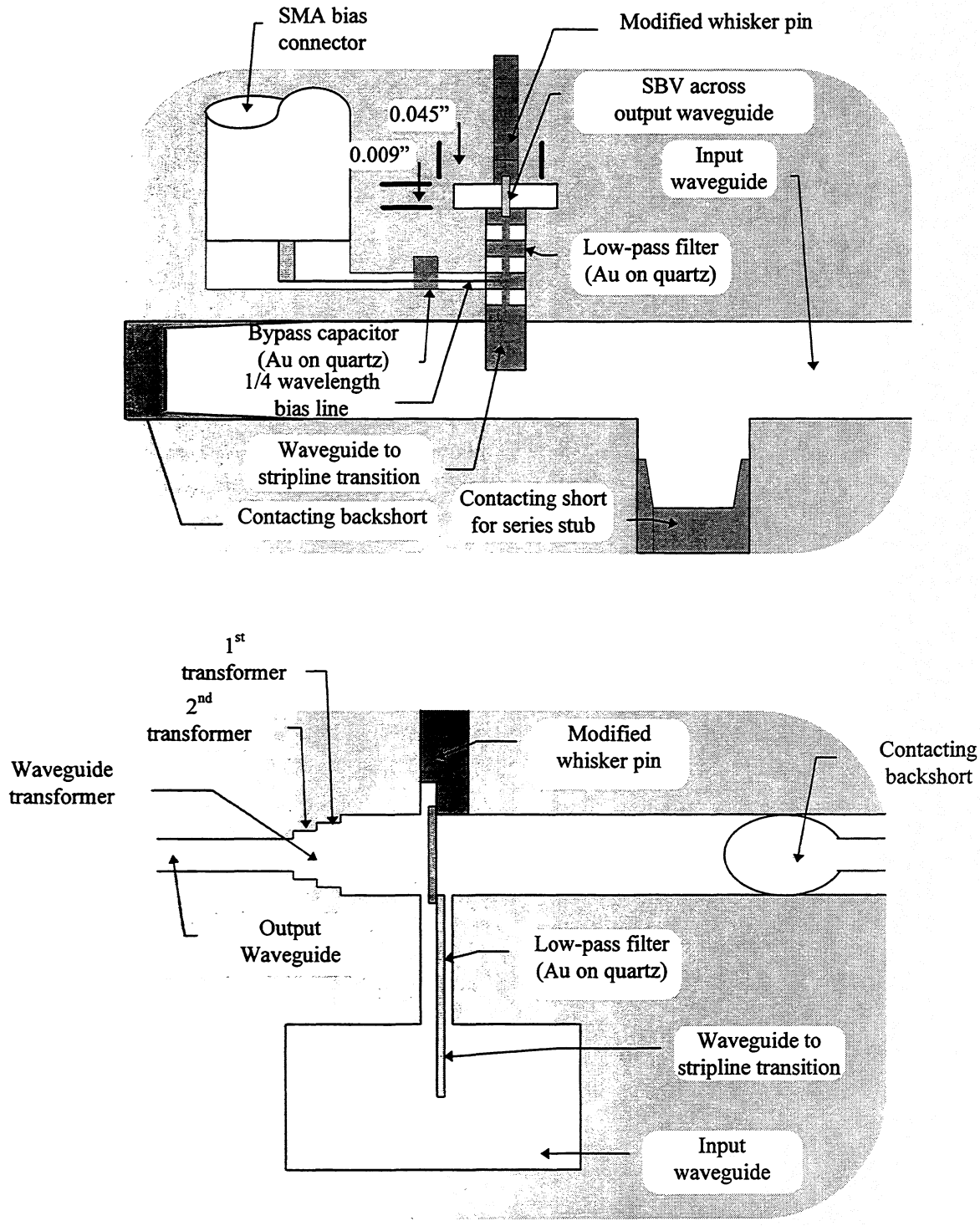

Figure 1 Schematic of the 200-290 GHz tripler waveguide structure showing (a) the block cross-section detailing the input waveguide and (b) the block cross-section detailing the output waveguide

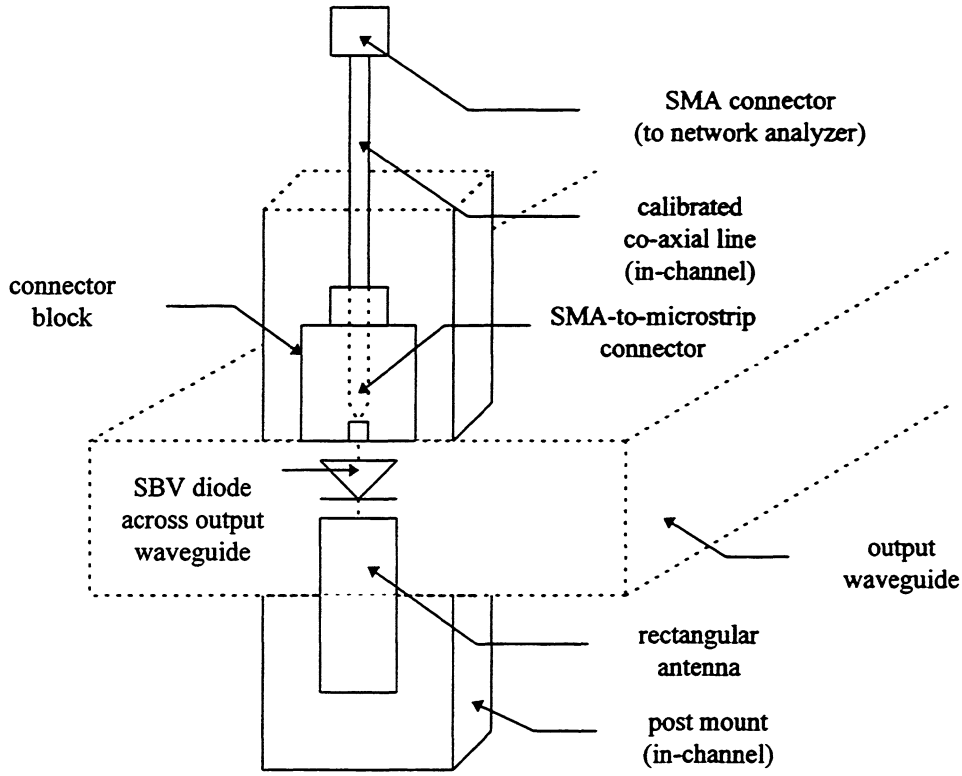

Figure 2 Cross-section of output waveguide structure

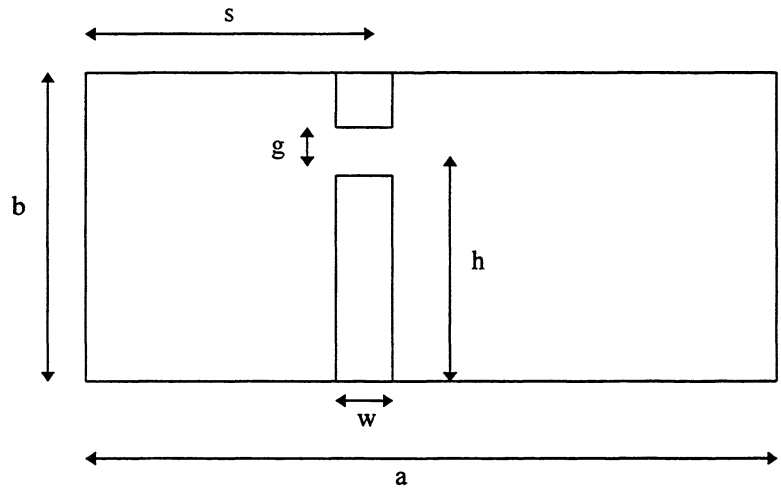

a = waveguide width
b = waveguide height
g= gap size
h = gap position (center of gap from bottom)
s = post position (center of post from side)
w = post width

Also,
s' = s / a = normalized post position
h' = h / b = normalized gap position
w' = w / a = normalized post width
g' = g / b = normalized gap size

Figure 3 Waveguide Mount Proposed by Eisenhart and Khan [1]

Because the tripler waveguide structure's embedding impedances versus backshort position can be decomposed into an analytical expression, this mounting block lends itself to rapid and accurate simulation. Software was written in Mathematica to solve equation (5) and the embedding impedance was calculated at the second, third, and fourth harmonics versus backshort position which were then used as inputs to the device simulators (which require the harmonic components of the linear embedding circuit). The calculated embedding impedances are shown in figure 4.

III. Numerical Device/Harmonic-Balance Simulation

The UVA 5M4 diode was used as the SBV in the tripler block with device parameters summarized in table 1. The UVA 5M4 diode is moderately doped and has a thin active layer which increases the device cut-off frequency and aids in high frequency tripling. However, the thin active layer also leads to low breakdown voltages and constrains the maximum input pump power relative to the embedding impedance for optimal efficiency. A cross-sectional schematic of the diode is presented in figure 5.

Table 1 Nominal Diode Parameters for the UVA 5M4

Diode	Diode Doping Density (cm^{-3})	Active Layer Thickness (μm)	Anode Diameter (μm)	Mobility (cm^2/Vs)
5M4	5.0×10^{16}	0.31	4.7	6200

In order to model the performance of the nonlinear active device in the linear embedding circuit, two independent CAD tools have been used. The first CAD tool is an equivalent circuit/harmonic-balance simulator (ECHB) based on the work of Siegel and Kerr [8]. The second is a large signal time- and temperature-dependent Drift-Diffusion Harmonic-Balance (DDHB) simulator [5]. For the ECHB, the Schottky Barrier Varactor (SBV) is modeled by its d.c. current versus voltage and d.c. capacitance versus voltage characteristics. This equivalent circuit model is then embedded into a harmonic-balance algorithm based on the multiple reflection technique [8] and the embedding impedances calculated as described above are incorporated. Although the ECHB technique is fast and has good convergence properties (converged solutions are on the order of five minutes on an IBM RS6000), analytical modeling techniques such as these do not provide a means for studying electron transport phenomena due to their macroscopic nature, and fail to accurately predict device performance at high frequencies [9]. This failure is attributed to the fact that equivalent circuit models cannot account for the actual physics of electron transport within the device. In particular, effects such as current saturation, velocity saturation, and transit time [6] phenomenon are not modeled using the ECHB code. Therefore, the novel physics-based Drift-Diffusion Harmonic-Balance simulator was employed.

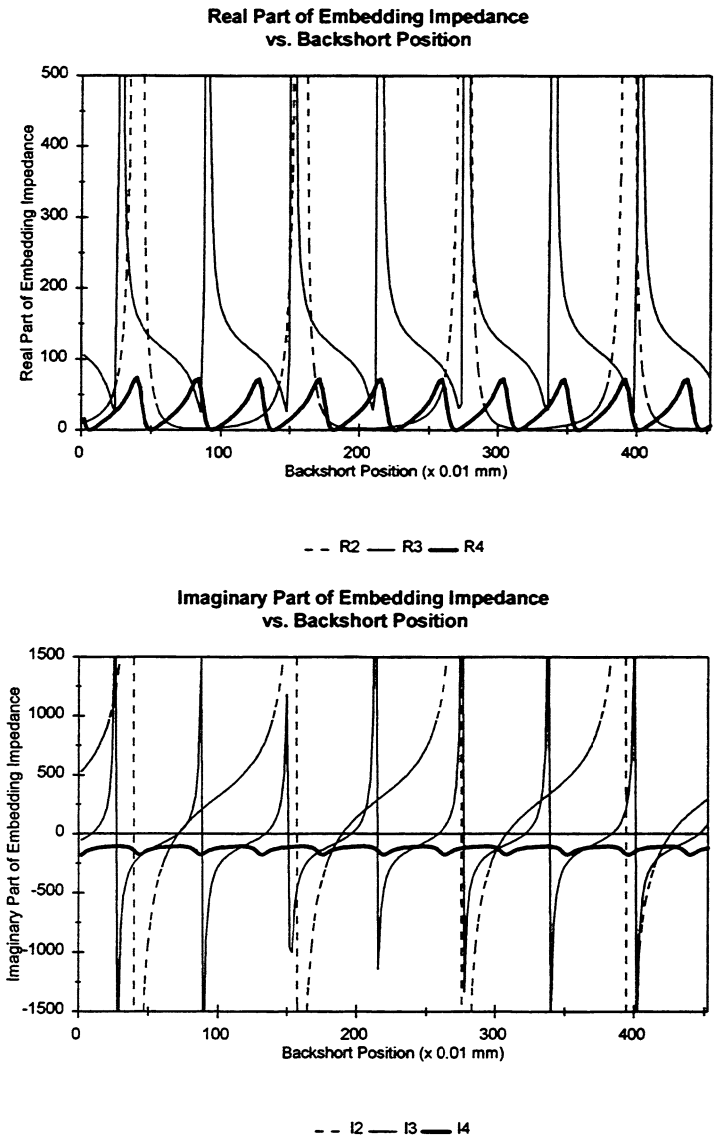

Figure 4 Calculated Embedding Impedances vs. Backshort Position

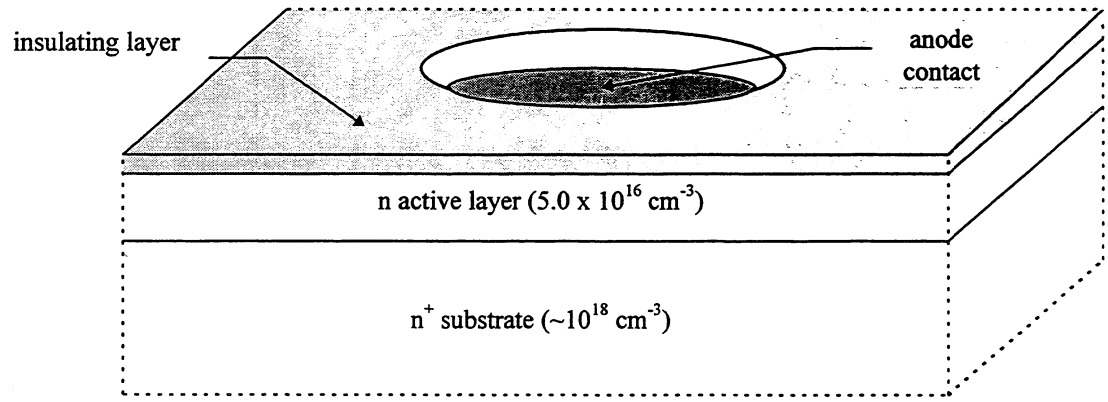

Figure 5 Typical cross-section of the UVA 5M4 GaAs SBV

Since this numerical device simulator self-consistently calculates the displacement and particle current throughout the entire device, the total electron current is accurately calculated. Carrier transport through the bulk region of the SBV is described [10] by a set of coupled nonlinear differential equations. This drift-diffusion analysis is based on the first two moments of the Boltzmann transport equation coupled to Poisson's equation. The resulting equations are

$$\frac{\partial n(x,t)}{\partial t} = \frac{1}{q}\frac{\partial J_n(x,t)}{\partial x}, \tag{6}$$

$$J_n(x,t) = q\mu_n(x,t)n(x,t)\frac{\partial \Phi_n(x,t)}{\partial x}, \tag{7}$$

and

$$\frac{\partial}{\partial x}\left[\varepsilon(x)\frac{\partial \Psi(x,t)}{\partial x}\right] = q\left[n(x,t) - N_D(x,t)\right], \tag{8}$$

where

$$n(x,t) = n_{i,ref}\exp\left[\frac{q}{kT}\left(\Psi(x,t) + V_n(x) - \Phi_n(x,t)\right)\right], \tag{9}$$

and where n is the electron density, q is the electron charge, J_n is the electron particle current density, Φ_n is the electron quasi-Fermi potential, Ψ is the electrostatic potential, $n_{i,ref}$ is the intrinsic electron density in the reference material (GaAs or InP), k is Boltzmann's constant, T is the absolute temperature, and V_n, μ_n, N_D, and ε are the spatially-dependent alloy potential [10], electron mobility, donor impurity concentration, and dielectric permittivity, respectively. Two types of mobility were considered for the simulations. First, a constant low field mobility derived from Monte Carlo simulations [11-12] was used. Second, in order to account for hot electron effects and high-field velocity saturation effects, a d.c. field-dependent mobility was computed as outlined in [13] using the Monte Carlo simulator of [11-12].

For accurate modeling of SBVs, current transport through the bulk device is combined with thermionic and thermionic-field emission current imposed at the metal-semiconductor contact. This approach is analogous to the analytical thermionic-emission/diffusion theory of Crowell and Sze [14]. Following the work of Adams and Tang [15-16], we have adopted a current density boundary condition at the metal-semiconductor interface which assumes a drifted Maxwellian electron distribution. This boundary condition allows us to avoid the unphysical accumulation of electrons at the metal-semiconductor interface near the flat-band voltage. The resulting current density interface constraint at x=0 is

$$J_n(0,t) = qv_{r,n}\left[n(0,t) - n_0\right] \tag{10}$$

where $n(0,t)$ is the electron density at the metal-semiconductor interface and n_0 is the equilibrium electron density at the interface. The effective surface recombination velocity for electrons is

$$v_{r,n} = v_d + \sqrt{\frac{2kT}{\pi m^*}} \left\{ \frac{\exp\left[-v_d^2\left(\frac{m^*}{2kt}\right)\right]}{1+\mathrm{erf}\left(v_d\sqrt{\frac{m^*}{2kT}}\right)} \right\} \tag{11}$$

where m^* is the effective electron mass at the metal-semiconductor interface. The amount of drift in the electron distribution at the metal-semiconductor interface is modeled as

$$v_d = \frac{J_n(0,t)}{qn(0,t)}. \tag{12}$$

The electrostatic potential at the metal-semiconductor interface, assuming a constant potential of zero for the metal is,

$$\Psi(0,t) = \frac{\chi_{ref} - \Phi}{q} \frac{kT}{q} \ln\left(\frac{N_{C,ref}}{n_{i,ref}}\right) \tag{13}$$

where χ_{ref} is the electron affinity in the reference material, Φ is the metal work function, and $N_{C,ref}$ is the total effective conduction band density of states in the reference material. The barrier height at the metal-semiconductor interface, Φ_b, is given by the first term in equation (11) multiplied by the electronic charge. This barrier height is lowered due to the Schottky effect by the amount

$$\Delta\Phi_b(t) = \sqrt{\frac{q|\xi(0t,)|}{4\pi\varepsilon(0)}} \tag{14}$$

where $\xi(0,t)$ is the electric field at the metal-semiconductor interface.

Through careful investigation of solution methods and the use of the one-dimensional state variables J_n, Φ_n, Ψ, *and* D we have developed a robust method with excellent numerical convergence and good speed. The carrier transport equations are solved for a given bias voltage, and subject to the metal-semiconductor (anode) interface constraints and an ohmic contact (cathode) boundary condition, using the coupled equation Newton-Raphson method (a one-dimensional finite difference analysis).

IV. Simulation Methodology

In order to simulate the performance of the SBV in the tripler block, the embedding impedances of the linear RF circuit were calculated using the model developed in Mathematica at 275 different output backshort positions for 0.01mm increments (as described in section II). Before beginning the set of 275 simulations for each CAD tool (ECHB & DDHB), each simulator required its own unique set of input specifications. A summary of the input parameters for the UVA 5M4 diode for each simulator (excluding the diode geometry) are provided in table 2.

Table 2 Inputs to the ECHB simulator

Barrier height (Φ)	-1.0 V
Current vs. Voltage curve fit parameter (η)	1.08
Capacitance vs. Voltage curve fit parameter (Γ)	0.5
Zero bias capacitance (C_0)	15×10^{-15} F
Saturation Current (I_{sat})	2.7×10^{-17} A
Series Resistance (R_s)	8.0 Ω
Input pump frequency (f_{in})	91.33 GHz
Input pump power (P_{in})	50.0 mW
d.c. bias (V_{dc})	-4.5 V

Inputs to the DDHB simulator

Barrier height (Φ)	-1.0 V
Number of time steps per period	501
Mobility	6200 cm^2/Vs for constant mobility simulations $\mu(\xi,t)$ for field-dependent simulations
Input pump frequency (f_{in})	91.33 GHz
Input pump power (P_{in})	50.0 mW
d.c. bias (V_{dc})	-4.5 V

Because the first harmonic embedding impedance is independently tunable from the higher harmonics using the two input tuners, a point of reference needed to be established to compare the experimental results with the CAD simulators. The chosen point of reference was at the point of experimental maximum third harmonic output power. The experimental embedding impedances for the second, third, and fourth harmonics at the chosen point of reference were calculated and the point of maximum simulated third harmonic output power was determined for each simulator. This point was found by iteratively conjugate matching the first harmonic embedding impedance to the determined intrinsic device impedance of the diode (solved for by each simulator) until the circuit embedding impedance was within 1% of the intrinsic device impedance. A conjugate match at the fundamental was chosen since the diode absorbs the maximum amount of available input power under conjugate match conditions, and a minimal amount of power is reflected. Table 3 presents the determined optimal first harmonic impedances for the three simulators

Table 3 Comparison of the determined first harmonic intrinsic device impedance

	ECHB	DDHB w/ constant low field mobility	DDHB w/ d.c. field-dependent mobility
First harmonic impedance	128 - j 292	49 - j 191	48 - j 186

V. Comparison of Experiment and Theory

After the inputs to each simulator were specified and the first harmonic embedding impedance for each simulator had been determined, simulations over a range of output backshort positions were performed (tuning backshort output waveguide section show in figure 1(b)). For both the ECHB and DDHB with d.c. field-dependent mobility simulators, simulations were performed over the 275 different backshort positions. After completing these simulations, sixty simulations were performed using the DDHB with

constant low field mobility simulator around the point of maximum third harmonic output power for comparison purposes. At a typical backshort position, a converged ECHB simulation was reached with one to two minutes and a converged DDHB (with either mobility function) simulation was reached in approximately five to ten hours (simulations were performed on an IBM RS6000).

For each simulation, the device was biased at -4.5 V and driven with 50 mW of available input power consistent with the experimental data (the reflected power at the LO port was minimized using the technique described above). The results of the measured power at the 275 different backshort positions are presented in figure 6 and compared with the predicted powers of the ECHB and DDHB with d.c. field-dependent mobility simulators.

As figure 6 illustrates, there is good agreement between both simulators and the measured data for relative power and spacing of the major power peaks. Although the relative magnitude of the major peaks is better predicted by the ECHB simulator, only the DDHB simulator with d.c. field-dependent mobility correctly predicts the power in the minor peaks.

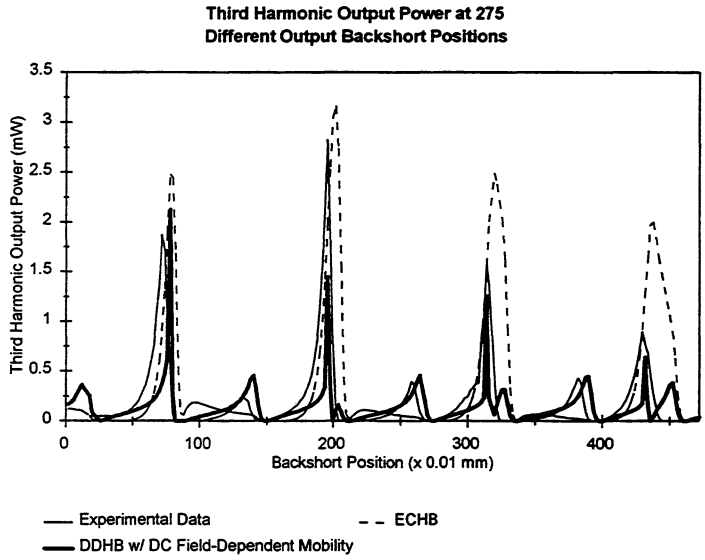

Figure 6 Comparison of predicted and measured third harmonic output power for the tripler block at 275 different output backshort positions

To better understand why the ECHB simulator fails to predict the minor peaks, a set of 60 different backshort positions spanning the second minor and major peaks was simulated using the DDHB simulator with constant low field mobility. Because the DDHB simulator with d.c. field-dependent mobility accurately predicts the relative power in the minor peaks, we wanted to investigate whether the dynamics of a field-dependent mobility gave rise to the power in the minor peaks or the modeling of electron transport was responsible. Figure 7 presents a comparison of the three simulators with the experimental data.

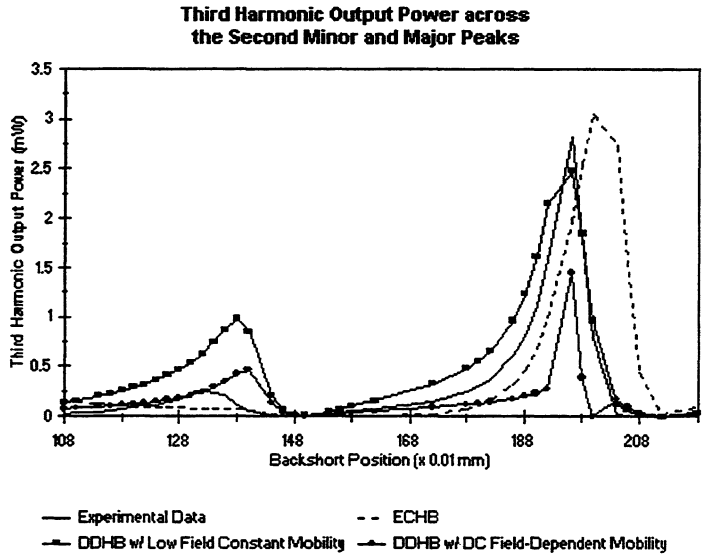

Figure 7 Comparison of predicted and measured output power for the tripler block for the ECHB and DDHB with d.c. field-dependent and constant low field mobilities over the second minor and major peaks

As can be seen from figure 7, the DDHB simulator with constant low field mobility correctly predicts and more accurately models the relative power in the minor peak. Also, the DDHB simulator with constant low field mobility more accurately predicts the relative power over the other simulators over the range of backshort positions. This suggests that the DDHB simulator with constant low field mobility most accurately predicts the performance of this tripler block. The ECHB simulator does not accurately reflect the relative power in the minor peaks due to the inaccurate determination of the diode impedance. Since there is a high degree of electron transport phenomenon occurring in the high doped short diode, the diode impedance is calculated at the wrong steady state phase and magnitudes of the voltage and current.

To determine the effect the calculated fourth harmonic embedding impedance (which has the most approximations made) had on the DDHB simulator with d.c. field dependent mobility, the set of 60 different backshort positions spanning the second major peak was re-simulated with the fourth harmonic embedding impedance shorted ($Z_4 = 0.1 + j0$). The results of these simulations are presented in figure 8. As illustrated by figure 8, the fourth harmonic impedance does not significantly affect the simulation results. This result supports the conclusion that the DDHB simulator with constant low field mobility most accurately predicts the performance of this tripler block.

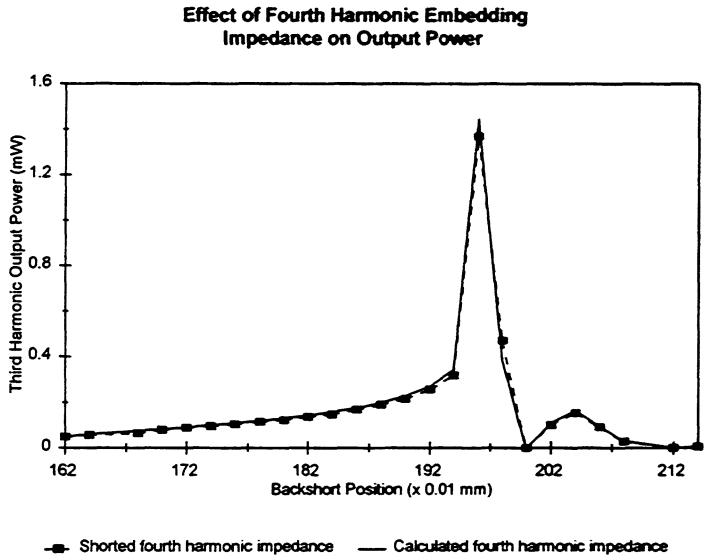

Figure 8 Effect of the fourth harmonic embedding impedance on third harmonic output power for the DDHB with d.c. field-dependent mobility over the second major peak

One set of final simulations was performed to determine the relationship between the first harmonic impedance and the third harmonic output power. These simulations were performed to determine the significance of the conjugate match specification at the first harmonic described earlier. Simulations were performed at the point of maximum third harmonic output power using the DDHB simulator with d.c. field-dependent mobility (for reasons of simulation speed) by changing only the real or imaginary part of the first harmonic impedance while leaving the unchanged part of the impedance set to that of table 4.3. The results of these simulations are shown in figure 9. As can be seen in figure 9, the point of maximum third harmonic output power is little affected by changes in either the real or imaginary parts of the first harmonic embedding impedance over some range of impedance values. This suggests some flexibility on the experimental setup of the tripler block for tuning at the LO.

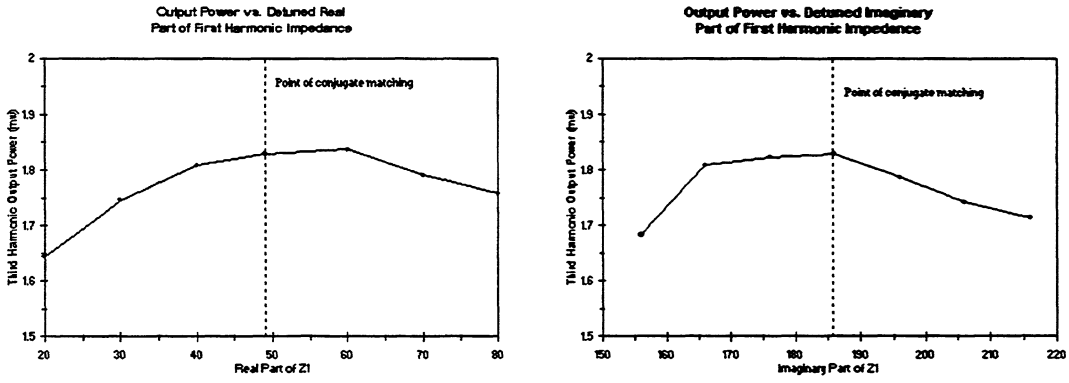

Figure 9 Comparison of maximum third harmonic output power vs. (a) real part of the first harmonic embedding impedance ($\mathrm{Im}\{Z_1\} = j186$) and (b) imaginary part of the first harmonic embedding impedance ($\mathrm{Re}\{Z_1\} = 49$)

VI. Simulation Results and Discussion

Once the comparison between the experimental data and the simulation results had been completed, an investigation of the ECHB and DDHB with d.c. field-dependent and constant low field mobility simulators was performed. All three simulators have the ability to generate steady-state current and voltage vs. time information. A comparison of the current vs. time and voltage vs. time at the second minor and major peaks of figure 6 are presented in figure 10. Although the ECHB simulator offers a significant advantage over its DDHB counterpart in terms of simulation time, there are significant limitations of the ECHB simulator. Both the ECHB and DDHB simulators provide current and voltage vs. time information, but only the DDHB simulator provides a means for studying the internal physics of device operation. Because of the microscopic nature of the DDHB simulator, both electron concentration and electric field across the device over time are solved for and are available as output. The numbers 1-5 on figure 10 represent instances where electron concentration and electric field vs. position were taken at the time corresponding to the number. Because the ECHB does not provide a means for analyzing these values, no numbers are listed on these plots. Figure 11 presents a comparison of the physics of device operation for the DDHB simulator with constant low field mobility and the DDHB simulator with d.c. field-dependent mobility at the second minor and major peaks.

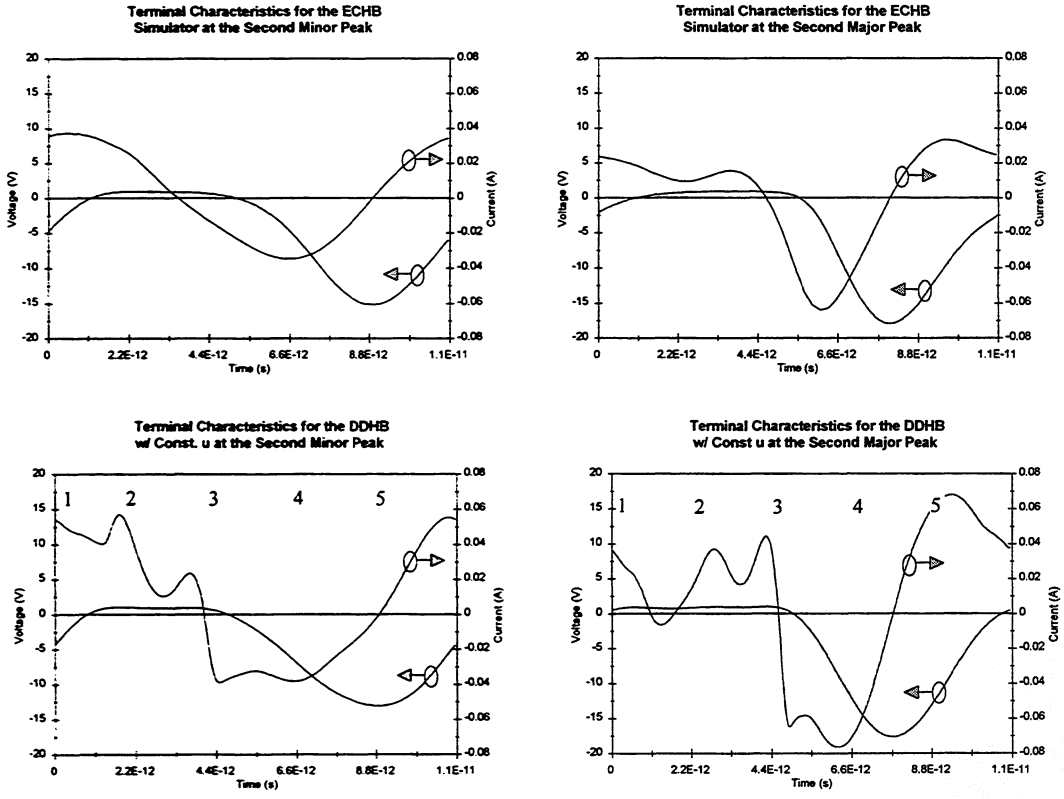

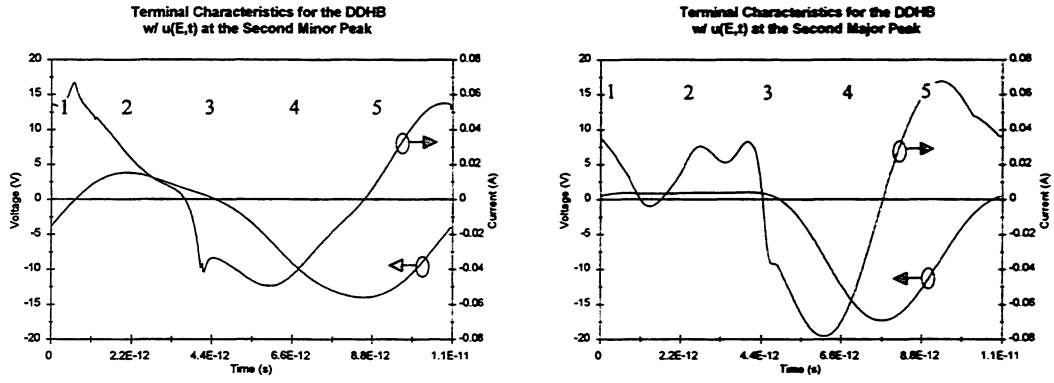

Figure 10 Comparison of the terminal characteristics for (a) the ECHB simulator (b) the DDHB simulator with constant low field mobility and (c) the DDHB simulator with d.c. field-dependent mobility at the second minor and major peaks

As can be seen from figure 10, both the ECHB and DDHB with d.c. field-dependent and constant low field mobility simulators predict similar output waveforms for the periodic voltage. The significant differences between the different simulators truly become apparent in the periodic current waveforms. Although the relative phase

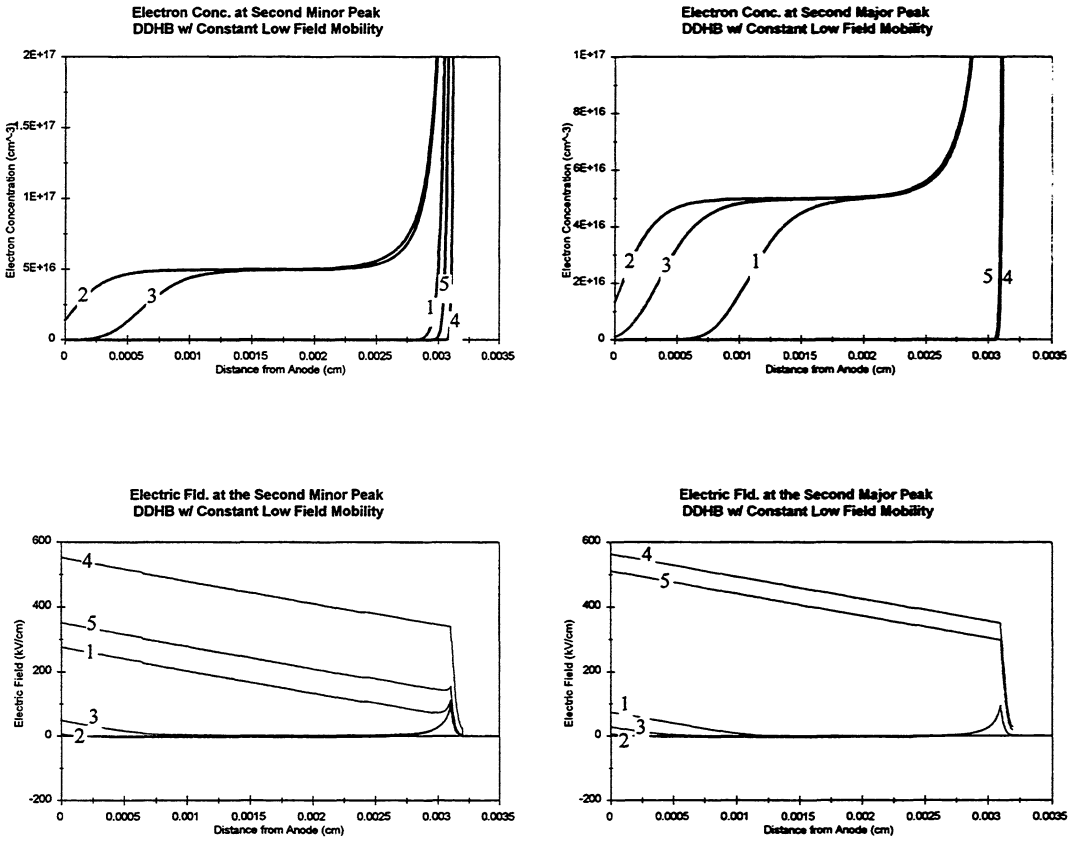

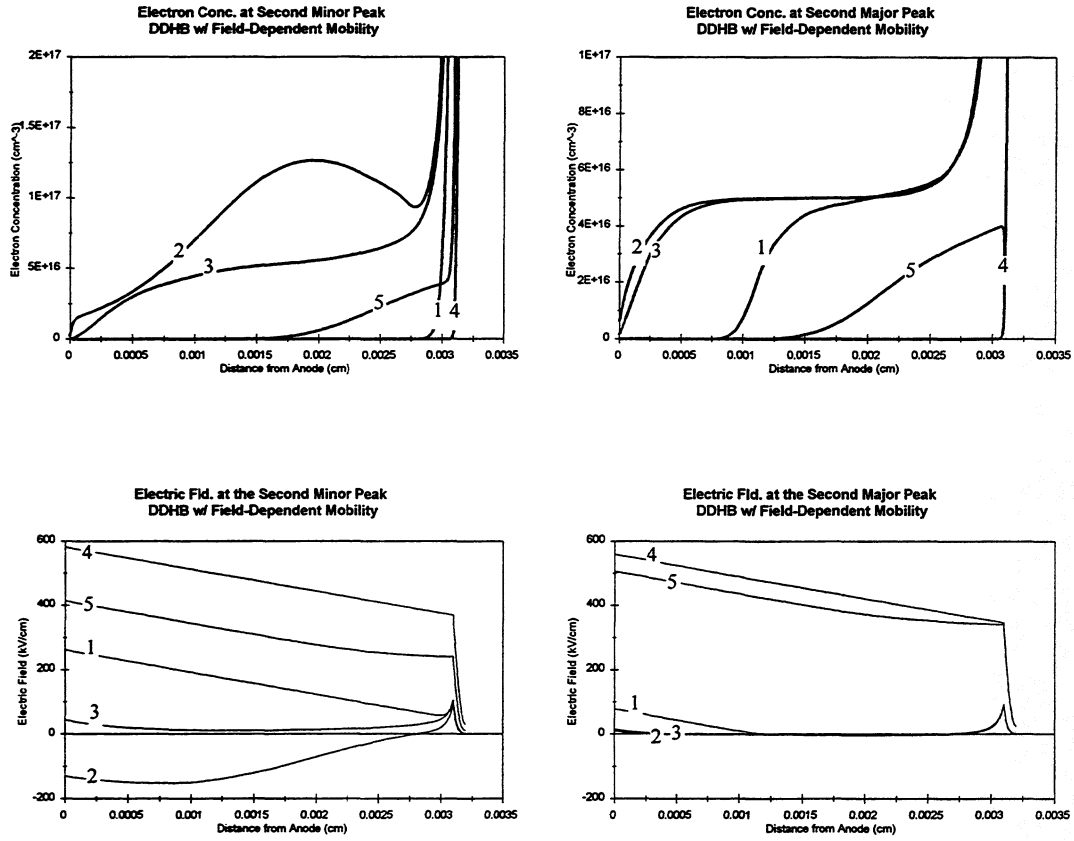

Figure 11 Comparison of electron concentration and electric field over the length of the active layer at five evenly spaced intervals over one period for both the second minor and major peaks for (a) DDHB with constant low field mobility and (b) DDHB with d.c. field-dependent mobility

differences between the voltage and current waveforms are similar for the different simulators, the ECHB simulator predicts a current waveform with fewer high frequency components and a lower peak to peak swing. Both the DDHB simulator with d.c. field-dependent mobility and constant low field mobility predict similar current waveforms with similar magnitudes. The relative maximums and minimums in the current waveform for the DDHB simulator with d.c. field-dependent mobility appear more exaggerated than that of the DDHB simulator with constant mobility. This exaggeration most likely arises from velocity saturation effects accounted for in the simulator which incorporates a non-static mobility with field-dependence.

Figure 11 demonstrates the power of the DDHB simulator for studying the physics of electron transport in the device. Both the DDHB simulator with d.c. field-dependent mobility and constant low field mobility predict that the device will fully deplete. The differences in the electron concentration gradients between the two different mobility models arise from velocity saturation effects [6]. As the magnitude of the voltage is increasing, the electrons towards the anode experience large electric fields (as seen in figure 11) but cannot reach the same velocity as the electrons towards the cathode so that weak electron concentration gradient across the depletion edge is created. The

depletion edge broadens as the faster electrons move toward the cathode. As the magnitude of the voltage is decreasing, the fast electrons in the low field region recompress the depletion edge. Also as the voltage decreases, the electron diffusion gradient is acting in the same direction as the movement of the electrons which helps create a sharp electron concentration gradient across the depletion edge. These gradient changes do not arise in the constant low field mobility model because there is no field dependence on the velocity and thus no saturation velocity.

The plots of the electric field vs. position over time in figure 11 illustrate that punch through occurs in the device (the electric field within the active layer does not go to zero) and that the fields become larger than the critical field (~500 kV/cm) for the device. This suggests that the device is being driven well in breakdown which may be limiting the tripling performance.

VII. Conclusions

In an attempt to handle the complex nature of tripler waveguide circuits, a tripler block incorporating the boundary conditions of Eisenhart and Khan was developed by Rutherford Appleton Laboratory. The boundary conditions of Eisenhart and Khan allow for the accurate analytical calculation of the linear RF embedding circuit impedances. A model was developed in Mathematica to calculate the embedding impedances at the second, third, and fourth harmonics as a function of the output backshort position. In order to simulate the performance of the active non-linear device in the linear embedding circuit, both equivalent circuit harmonic-balance (ECHB) and drift-diffusion harmonic-balance (DDHB) CAD tools were used. The ECHB simulator offers superior solution times (on the order of 100 times faster than the DDHB simulator). The self-consistent DDHB simulator both with d.c. field-dependent mobility and constant low field mobility offers the ability to study the internal physics of electron transport in the active non-linear device. Since these CAD tools require the embedding impedances as inputs to the simulator, the accurate nature of the calculations made in Mathematica were made possible by the Eisenhart and Khan boundary condition specifications. The ECHB and DDHB simulators were used to simulate the performance of the tripler block over a wide range of output backshort positions. The results of these simulations were compared with experimental measurements made over the same set of backshort positions. The results suggest that although the ECHB simulator can accurately predict the experimental data at some backshort positions, only the DDHB simulator can accurately predict the tripler block performance over a wide range of output backshort positions. This is a direct result of the inability of the ECHB simulator to accurately predict the diode impedance; hence the phase and magnitudes of the steady state voltage and current are incorrect as the embedding circuit impedance varies. For the first time, the combination of the analytical model specifying the linear RF circuit and an accurate self-consistent CAD tool simulating the active non-linear device in the linear RF circuit can accurately predict the performance of a millimeter wave tripler block. This combination has for the first time allowed for a complete analysis of a tripler block.

Acknowledgments

This research has been sponsored by NSF grant #ECS-9412931. The authors greatly appreciate many important discussions with Tom Crowe, Rob Jones, and Greg Tait.

References

[1] John Thornton, "An Analytical Model for a Rectangular Antenna in Metallic Enclosure and its use for the Optimization of a 250 GHz Source for Antenna Characterization," July 1996, p. 1-3.

[2] P. Zimmermann, "Frequency Multipliers and LO Sources for the Submillimeter Wave Region," Proc. ESA Workshop on Millimeter Wave Tech. and Appl., Dec. 1995.

[3] P. J. Koh, W. C. B. Peatman, T. W. Crowe, Neal R. Erickson, "Novel Planar Varactor Diodes," 7th Int. Symp. Space THz Technology, March 1996.

[4] R. L. Eisenhart and P. J. Khan, "Theoretical and Experimental Analysis of a Waveguide Mounting Structure," *IEEE Trans. on Microwave Theory and Tech.*, Vol. 19, No. 8, August 1971.

[5] J. R. Jones, "CAD of Millimeter Wave Frequency Multipliers: An Experimental and Theoretical Investigation of the Heterostructure Barrier Varactor," Doctoral Dissertation, University of Virginia, January 1996.

[6] R. E. Lipsey, S. H. Jones, J. R. Jones, T. W. Crowe, L. F. Horvath, U. V. Bhapkar, and R. J. Mattauch, "Monte Carlo Harmonic-Balance and Drift-Diffusion Harmonic-Balance Analyses of 100-600 GHz Schottky Barrier Varactor Frequency Multipliers," Submitted to *IEEE Electron Dev.*, November 1996.

[7] J. W. Archer, "An Efficient 200-290 GHz Frequency Tripler Incorporating a Novel Stripline Structure," *IEEE Trans. on Microwave Theory and Tech.*, Vol. 32, No. 4, April 1984.

[8] P. H. Siegel, A. R. Kerr, and W. Hwang, "Topics in the Optimization of Millimeter-Wave Mixers," NASA Technical Paper 2287, 1984.

[9] J. R. Jones, S. H. Jones, G. B. Tait, "Self-Consistent Physics Based Numerical Device/Harmonic-Balance Circuit Analysis of Heterostructure Barrier and Schottky Barrier Varactors including Thermal Effects," *Proceedings of the Sixth International Symposium of Space Terahertz Technology*, March 1995, p. 423.

[10] E. L. Kollberg, T. J. Tolmunen, M. A. Frerking, and J. R. East, "Current Saturation in Submillimeter Wave Varactors," *IEEE Trans. on Microwave Theory Tech.*, Vol. 40, No. 5, May 1992, pp. 831-838.

[11] U. V. Bhapkar, "Monte-Carlo Simulation of GaAs Schottky Diodes for Terahertz Frequencies," Doctoral Dissertation, University of Virginia, 1995.

[12] U. V. Bhapkar and R. J. Mattauch, "Monte Carlo Simulation of Terahertz Frequency Schottky Diodes," *Proceedings of the 1995 International Semiconductor Device Research Symposium*, Vol. 1, Dec. 1995, pp. 263-265.

[13] M. F. Zybura, S. H. Jones, G. B. Tait and J. R. Jones, "100-300 GHz Gunn Oscillator Simulation through Harmonic Balance Circuit Analysis Linked to a Hydrodynamic Device Simulator," *IEEE Microwave Guided Wave Lett.*, Vol. 4, No. 8, August 1994, p. 282.

[14] C. R. Crowell and S. M. Sze, "Current Transport in Metal-Semiconductor Barriers," *Solid-State Electron*, Vol. 9, No. 11/12, Nov./Dec. 1966, pp. 1035-1048.

[15] J. Adams and T. W. Tang, "A Revised Boundary Condition for the Numerical Analysis of Schottky Barrier Diodes," *IEEE Electron Dev. Lett.*, Vol. 7, No. 9, Sept. 1986, pp. 525-527.

[16] J. Adams and T. W. Tang, "Computer Simulation of Boundary Conditions for Schottky Diodes," *Elec. Lett.*, Vol. 25, No. 16, Aug. 1989, pp. 1098-1100.